Check for updates

ChemCatChem
Research Article
doi.org/10.1002/cctc.202501430
Chemistry Europe
European Chemical Societies Publishing
www.chemcatchem.org

Tuning Potassium Concentration in Empowered Supports for Fischer-Tropsch Synthesis

Oaitse Percy Ketlogetswe,[a] Motlokoa Khasu,[a] Wijnand Marquart,[a] Charalampos Drivas,[b, c] Evangeline B. McShane,[d] Simon A. Kondrat,[d] Gabriela Grzybek,[e] Paweł Stelmachowski,[e] Andrzej Kotarba,[e] Michael Claeys,[a] and Nico Fischer*[a]

Potassium substitution in the A site of a $LaAl_{0.8}Mn_{0.2}O_{3-\delta}$ perovskite was investigated as a strategy to anchor the promoter within a crystalline matrix thus suppressing its mobility under reaction conditions and enhancing the performance of iron-based Fischer-Tropsch (FT) catalysts. A series of $La_{1-x}K_xAl_{0.8}Mn_{0.2}O_{3-\delta}$ (x = 0 to 8 at.%) perovskites was prepared and subsequently loaded with pre-synthesized iron oxide nanoparticles. Quantitative in situ X-ray diffraction revealed that potassium incorporation delays the reduction of the Fe_3O_4 phase and accelerates the rate of carburization, resulting in a higher crystalline iron carbide content at increased potassium concentrations. Under low temperature FT conditions (240 °C, 15 bar, $H_2/CO = 2$) CO conversion and CO_2 selectivity increased with potassium loading, while C_5+ selectivity peaked at 2 at.% potassium in the A site of the perovskite lattice. At the same loading, thermal alkali desorption and X-ray absorption spectroscopy studies revealed that potassium remains strongly anchored within the lattice yet sufficiently electronically active to enhance CO activation without over-promoting the water-gas shift (WGS) reaction, thereby maximizing chain growth selectivity. These results highlight the potential of fine-tuning concentrations of promoters in empowered supports to optimize catalyst performance, offering a stable and controllable alternative to conventional deposition or impregnation methods.

1. Introduction

The Fischer-Tropsch (FT) synthesis is a key pathway for converting synthesis gas (H_2/CO), derived from coal, biomass, or CO_2, into liquid hydrocarbons. This process is gaining renewed interest as a promising route for sustainable fuel production. Iron-based catalysts are reported to be effective for processes with H_2 lean synthesis gas ($H_2/CO < 2$) due to their potential activity for the water-gas shift (WGS) reaction. Although the WGS activity produces CO_2 as a by-product, iron catalyst remains attractive for their low cost, natural abundance of raw materials, and comparatively low methane selectivity. More recently, iron has also been explored as catalyst for the direct CO_2 hydrogenation through the reverse WGS reaction. However, the challenge for the commercial iron-based FT catalysts is the stability of the active phases under intensified FT conditions (elevated temperatures, pressures, and high partial pressures of water). Under these reaction conditions, the metallic Fe phase is unstable and transforms into a metastable mixture of carbides and oxides, with the latter resulting in deactivation under high conversion conditions.[1,2] The catalysts are commonly promoted to improve catalyst reducibility, formation of the carbide phase, stability, and activity. Alkali metal compounds such as potassium and sodium are particularly effective. Manganese has also been discussed as stabilising the catalyst and increasing the selectivity to short-chained olefins, while copper is widely used as a reduction promoter.[3–5] The presence of alkali promoters specifically, influences the reduction/carbide formation and performance of the iron-based catalyst by increasing the adsorption energy of CO and weakening the strength of the C–O bond through modification of the electron density around the active site. This affects the concentration of carbon and hydrogen species on the catalytic surface, consequently leading to the enhanced carburization,[6] improved activity, and selectivity.[7]

However, if the optimum concentration of the alkali promoter is surpassed, the carbon formation rate becomes too fast, leading to carbon deposition on the surface and deactivation of the catalyst.[6] It is for this reason that promoters

---

[a] *O. P. Ketlogetswe, M. Khasu, W. Marquart, M. Claeys, N. Fischer*
Catalysis Institute in the Department of Chemical Engineering, University of Cape Town, Rondebosch, Cape Town 7700, South Africa
E-mail: nico.fischer@uct.ac.za

[b] *C. Drivas*
Cardiff Catalysis Institute, School of Chemistry, Cardiff University, Cardiff CF10 3AT, UK

[c] *C. Drivas*
UK Catalysis HUB, Research Complex at Harwell, Science and Technology Facilities Council, Rutherford Appleton Laboratory, Didcot OX11 0FA, UK

[d] *E. B. McShane, S. A. Kondrat*
Department of Chemistry, Loughborough University, Loughborough LE11 3TU, UK

[e] *G. Grzybek, P. Stelmachowski, A. Kotarba*
Faculty of Chemistry, Jagiellonian University, Krakow 30387, Poland

Supporting information for this article is available on the WWW under https://doi.org/10.1002/cctc.202501430

© 2025 The Author(s). ChemCatChem published by Wiley-VCH GmbH. This is an open access article under the terms of the Creative Commons Attribution License, which permits use, distribution and reproduction in any medium, provided the original work is properly cited.

© 2025 The Author(s). ChemCatChem published by Wiley-VCH GmbH

such as potassium are usually reported to have an optimum concentration, above which further addition becomes detrimental to the catalyst performance.[8] Pendyala et al.[9] observed that while a moderate potassium loading of 0.5% (atomic ratio relative to iron) enhanced catalyst stability and increased C_{5+} hydrocarbons production, excess potassium ($>$ 2% atomic ratio) led to accelerated deactivation. Interestingly, the unpromoted and excessively Kloaded (2 K/100Fe) catalysts exhibited similar deactivation trends over time, even though the deactivation mechanisms may differ. The authors noted that the unpromoted catalysts likely deactivate through oxidation of active Fe carbides and carbon layer formation, whereas excessive promotion accelerates carbon deposition via rapid carbide formation and surface site blocking.[9] A further challenge in using potassium as a promoter is its mobility under reaction conditions. Studies have shown that potassium undergoes significant surface migration, leading to redistribution, clustering or ultimately loss of the promotional effect.[10–12] This mobility disrupts uniform promoter coverage, weakens the intended promotional effects, and undermines the catalyst stability, activity, and selectivity. These obstacles underscore the necessity to develop new strategies to effectively immobilise potassium, avoiding overpromotion, and enhancing catalyst performance under FT conditions.

One promising approach, we have reported on previously, is to structurally integrate potassium into the catalyst carrier and in such creating empowered supports.[13] Perovskites have emerged as an attractive materials for this purpose, due to their ability to accommodate a wide range of cation substitutions while maintaining their structural integrity.[14–16,17] Recently, Khasu et al.[13] demonstrated the successful synthesis of perovskites incorporating promoting elements, Mn and K, within their crystal lattice to fulfil the classic role of a support in conjunction with promoting functionalities. In their study, a series of $LaAlO_{3-\delta}$ perovskite catalysts were prepared by partially substituting La with 10 at.% K in the A site and substituting Al in the B site with varying amounts of Mn (0, 10, 20, 60, and 100 at.%). Potassium incorporation into the perovskite lowered the reduction temperature from Fe_2O_3 to Fe_3O_4 and accelerated the rate of iron carbide formation. Among the compositions investigated, the catalyst containing 10 at.% K and 20 at.% Mn ($La_{0.9}K_{0.1}Al_{0.8}Mn_{0.2}O_{3-\delta}$) achieved a 60% higher CO conversion than an analogous catalyst with potassium added via conventional impregnation, while simultaneously lowering the undesired CH_4 and CO_2 selectivity. Notably, the perovskite lattice remained structurally intact during reaction, an indication of stability with no measurable loss of promoters. These findings led to a strong motivation to investigate whether the K loadings could be further optimized.

The present study focuses on the effect of lower ($<$ 10 at.%) potassium loadings in the perovskite structure. A series of $La_{1-x}K_xAl_{0.8}Mn_{0.2}O_{3-\delta}$ perovskites were synthesized, in which La is substituted with K, while maintaining a fixed Al and Mn concentration (80 and 20 at.%, respectively) in the B site. By supporting iron oxide (Fe_3O_4) nanoparticles on these perovskites with systematically varied potassium content, we investigate how decreasing potassium loading affects the reducibility of iron, its carbide formation, and the FT performance, with the aim of identify the optimum potassium concentration for an enhanced FT synthesis.

2. Results and Discussion

2.1. Characterisation of Catalysts

Transmission electron microscopy (TEM) micrographs showed near-spherical Fe_3O_4 nanoparticles with a relatively narrow size distribution of 7 – 11 nm with an average particle diameter of 8 ± 1 nm (see Figure S1a). The volume-weighted mean diameter was calculated as approximately 8 ± 1 nm. X-ray diffraction confirmed the formation of pure Fe_3O_4 matching the reference pattern of magnetite (see Figure S1b), with Rietveld refinement yielding an average crystallite size of 8 nm. The theoretical surface area was calculated to be 145 m^2/g, slightly higher than the measured value of 130 m^2/g, likely due to mild agglomeration (Table S1).

All synthesized potassium-substituted lanthanum aluminates have the same rhombohedral crystal structure with space group R-3c matching the $LaAlO_3$ perovskite reference, PDF-5 + 04–012–6135 (see Figures 1a and S2a). A progressive shift of reflections to higher values of 1/d (by 0.011 $Å^{-1}$) is observed, with the shift becoming more pronounced at K loadings above 2 at.% (see Figures 1b and S2b). This behavior indicates lattice expansion due to substitution of La^{3+} by the larger K^+ ion, supporting the assumption of successful incorporation of the potassium into the crystal lattice. Cimino et al.[18] attributed similar shifts to an increase in the unit cell volume with higher alkali content. Additionally, a progressive decrease in intensity and broadening of the reflections with increasing potassium content suggests a reduction in average crystallite size (see Figures 1b and S2b). Bulk compositions of the samples determined by ICP-OES confirmed that the measured K loadings closely match the intended target compositions (see Table S2).

Specific surface areas of the synthesized perovskites ranged from 12–31 m^2/g (see Table 1 and Table S3), with potassium-containing samples consistently exhibiting higher values than the unpromoted $LaAl_{0.8}Mn_{0.2}O_{3-\delta}$ (K-0). A notable increase in BET surface area was observed following deposition of Fe3O4 nanoparticles. This increase can be attributed to the addition of the iron oxide particles onto the very low surface area of the perovskite. Due to the absence of notable porosity, the nanoparticles contribute significantly to the overall surface area and no reduction of surface area due to pore blockage is measured. The measured Fe_3O_4 loadings are between 15 and 19 wt.%, in good agreement with the nominal 20 wt.% target. XRD confirmed the successful deposition of the nanoparticles, PDF-5 + 04–015–9120, with no new phases or changes in the perovskites structure observed (see Figure S3).

The structural evolution of the iron species during reductive treatment was monitored with in situ XRD. For the unpromoted catalyst (K-0), the initial transformation of Fe_3O_4 to metallic Fe was recorded at 287 °C, with the full reduction achieved at 351 °C

© 2025 The Author(s). ChemCatChem published by Wiley-VCH GmbH

18673899, 0, Downloaded from https://chemistry-europe.onlinelibrary.wiley.com/doi/10.1002/cctc.202501430 by NICE, National Institute for Health and Care Excellence, Wiley Online Library on [13/01/2026]. See the Terms and Conditions (https://onlinelibrary.wiley.com/terms-and-conditions) on Wiley Online Library for rules of use; OA articles are governed by the applicable Creative Commons License

18673899, 0, Downloaded from https://chemistry-europe.onlinelibrary.wiley.com/doi/10.1002/cctc.202501430 by NICE, National Institute for Health and Care Excellence, Wiley Online Library on [13/01/2026]. See the Terms and Conditions (https://onlinelibrary.wiley.com/terms-and-conditions) on Wiley Online Library for rules of use; OA articles are governed by the applicable Creative Commons License

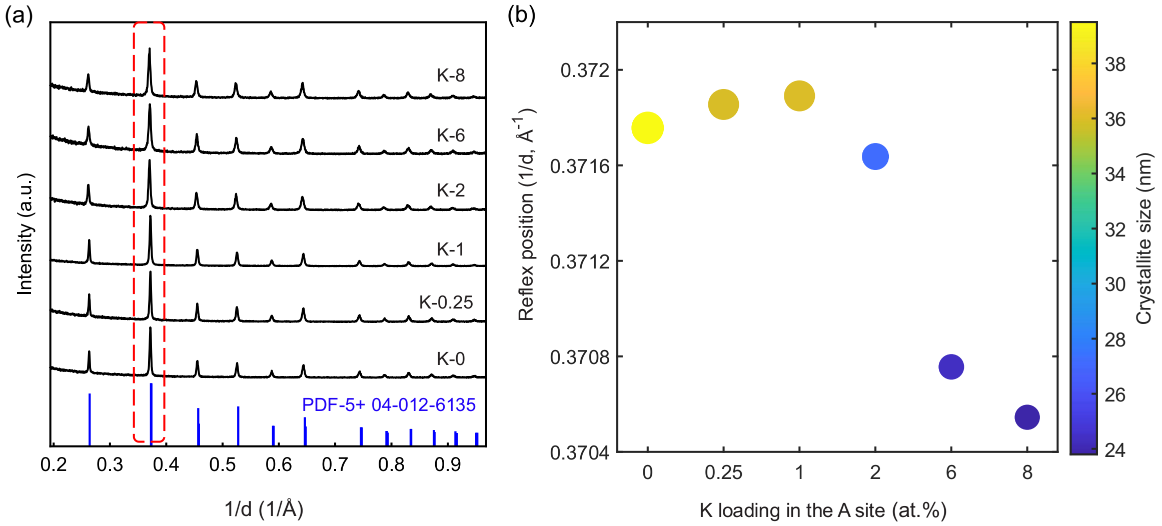

Figure 1. a) XRD patterns of the as-synthesized $La_{1-x}K_xAl_{0.8}Mn_{0.2}O_{3-\delta}$ perovskites confirming successful synthesis as evidenced by reference pattern of $LaAlO_3$ perovskite and b) reflex position of the (110) plane as a function of K loading in the A site (at.%).

Table 1. Properties of as-synthesized perovskites before and after Fe_3O_4 nanoparticles deposition. BET surface area of the as synthesized perovskites and after loading Fe_3O_4 nanoparticles. Total iron loading as analyzed via ICP-OES and calculated loading of Fe_3O_4 based on ICP-OES data.

Catalyst	BET surface area (m^2/g) Perovskites as synthesized	BET surface area (m^2/g) Fe_3O_4 NPs supported on Perovskites	Measured Fe^0 loading (wt.%)	Calculated Fe_3O_4 loading (wt.%)
K-0	12	36	12.5	17.3
K-0.25	12	36	13.6	18.8
K-1	18	39	12.9	17.8
K-2	23	44	13.6	18.8
K-6	31	46	13.8	19.1
K-8	34	48	11.0	15.2

(Figure 2a). Rietveld refinement showed a gradual decline in the Fe_3O_4 phase from an initial 17 wt.%, which is in good agreement with the 18 wt.% Fe_3O_4 determined by ICP-OES, to full reduction in 2.5 h (Figure 2c). The resulting metallic Fe content remained at 12 wt.% at 450 °C. Upon exposure to FT reaction conditions, the formation of an iron carbide phase, modelled in the Rietveld analysis as cementite, ε-Fe_3C, was observed after 36 min (Figure 2b). This was accompanied by a steady decrease in the concentration of metallic Fe, which was fully transformed to the carbide after approximately 1.5 h under syngas atmosphere. Quantitative phase analysis confirmed the progressive carburization of metallic Fe, with the carbide phase remaining constant at 14 wt.% after 3 h, indicating complete transformation of the metallic Fe (Figure 2d).

The catalysts K-2 and K-8 showed a delayed reduction, with the onset of Fe° formation between 319 and 330 °C, respectively (Figures 3a and S4a). No oxide phase is observed beyond 393 °C (K-2) and 404 °C (K-8). This delayed reduction in the presence of potassium is consistent with literature reports and is attributed to the effect of strong K–Fe–O interactions which hinder dissociative H_2 adsorption and slow oxygen removal.[19,20] Under FT reaction conditions, the potassium-containing catalysts showed an accelerated carburization. The carbide phase could be observed after just 15 min for K-2 and within the first 10 min for K-8, compared to the 36 min for K-0 (Figures 3b and S4b). This faster carburization agrees with literature findings that potassium enhances CO dissociation and increases C availability on the iron surface, while suppressing hydrogen adsorption, thereby promoting faster and complete iron carburization.[9,19]

In the K-2 catalyst, the Fe_3O_4 phase decreased from an initial 20 wt.% during reduction, with metallic Fe forming and maintained at approximately 14 wt.% following complete transformation in 2.8 h, in good agreement with the Fe° content determined by ICP-OES (Figure 3c). Upon exposure to syngas, the metallic Fe phase diminished rapidly, until it was fully transformed after approximately 1 h, while the carbide phase concurrently formed and remained constant at about 16 wt.% (Figure 3d). At a higher potassium loading, K-8, Fe_3O_4 decreased from 17 wt.% to zero during reduction and the resulting metallic Fe persisted at about 15 wt.% in 2.9 h (Figure S4c). This value notably exceeds the 11 wt.% Fe^0 measured by ICP-OES,

© 2025 The Author(s). ChemCatChem published by Wiley-VCH GmbH

18673899, 0, Downloaded from https://chemistry-europe.onlinelibrary.wiley.com/doi/10.1002/cctc.202501430 by NICE, National Institute for Health and Care Excellence, Wiley Online Library on [13/01/2026]. See the Terms and Conditions (https://onlinelibrary.wiley.com/terms-and-conditions) on Wiley Online Library for rules of use; OA articles are governed by the applicable Creative Commons License

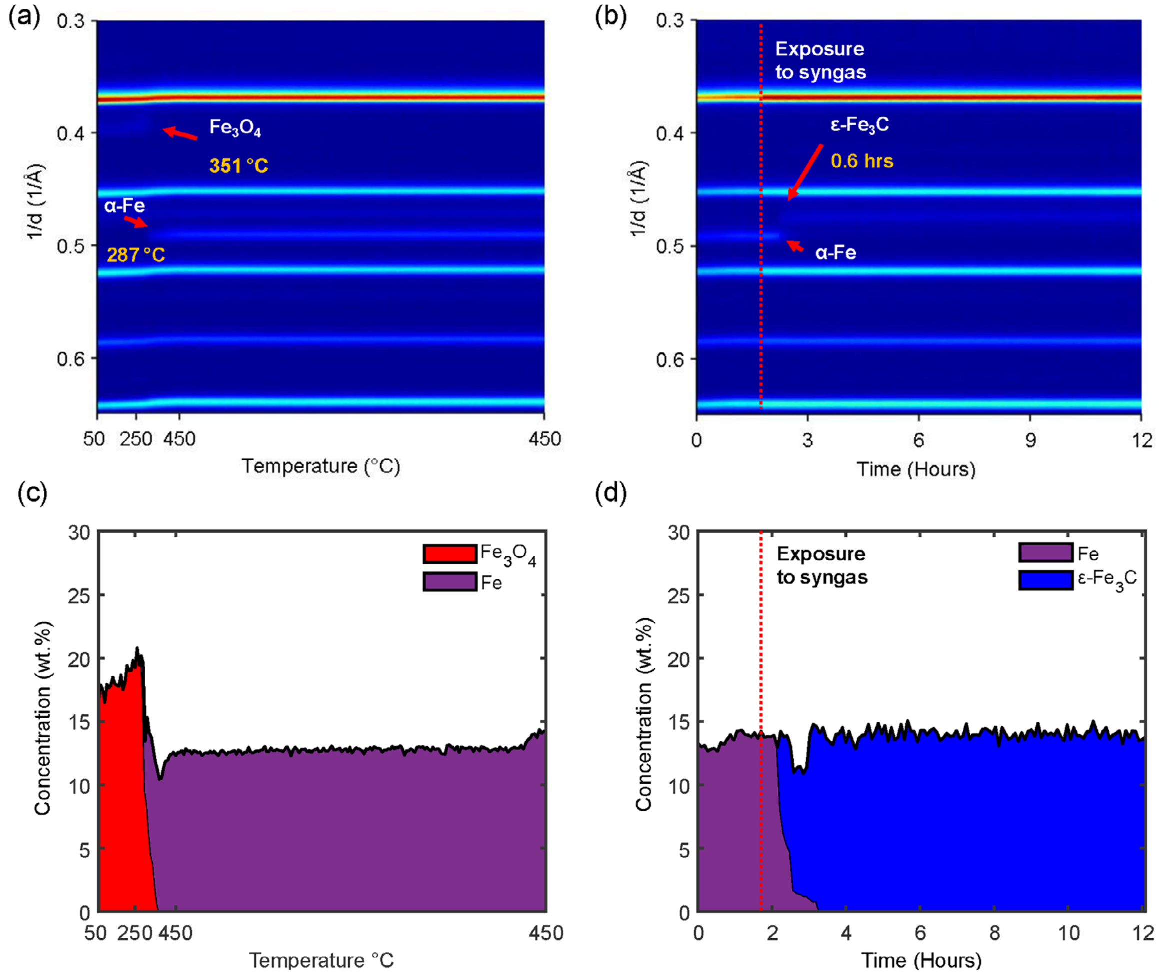

Figure 2. On-top view of XRD patterns collected as function of temperature and time. a) Reduction (H_2 flow, 450 °C, 15 h) and b) carburization ($H_2/CO = 2$, 240 °C, 15 bar) behavior of the unpromoted catalyst, K-0. c) The phase composition during reduction and d) carburization as calculated via Rietveld refinement is provided. All unlabeled reflections in (a & b) correspond to the perovskite phase. For clarity, the concentration of the perovskite phase is omitted in figure (c & d).

which corresponds to a theoretical maximum Fe_3O_4 content of approximately 15 wt.%. A similar overestimation is observed for the final Fe_3C content, which was retained at approximately 15 wt.% upon complete carburization (Figure S4d). These discrepancies likely stem from limitations in the refinement, as the limited signal-to-noise ratio in the in situ XRD scans, a result of the high temporal resolution, makes a quantitative analysis challenging.

In addition to phase quantification, Rietveld refinement also provided insights into the crystallite size evolution of the iron species (Table 2). While the initial Fe_3O_4 crystallite sizes were similar across all samples, around 8 nm, notable differences emerged after reduction and carburization. The unpromoted catalyst, K-0, formed the largest α-Fe crystallites (approximately 19 nm). The moderately promoted K-2 catalyst also yielded larger Fe^0 of around 18 nm, whereas K-8 catalyst supports much smaller iron crystallites of 10 nm. However, after carburization the carbide crystallites in all samples converge to a similar size range of approximately 8 nm, regardless of potassium loading. This suggests that the final carbide crystallite size is relatively insensitive to potassium loading and when the reduced Fe domains are larger, a significant decrease in size proceeds during the incorporation of carbon. On the contrary, for smaller metallic Fe crystallite sizes essentially no change in size is observed. This contrasts the findings of Chang et al.[21] who reported increased carbide crystallite sizes with higher potassium loadings in silica supported catalyst.

The increase in crystalline size after reduction is attributed to sintering of metallic Fe particles as Fe_3O_4 is converted to α-Fe under H_2 at elevated temperatures. Subsequent carburization leads to the formation of iron carbides, during which carbon diffusion into the metallic lattice induces structural strain and fragmentation of larger metallic crystallites into smaller carbide domains. As a result, the apparent crystallite size decreases significantly, consistent with literature reports reporting on the generation of multiple small crystalline domains within a single particle.[22]

Prior to catalytic testing in the slurry reactor, all catalysts were activated in a quartz tube reactor under conditions similar to those used in the in situ XRD reduction experiments. To confirm the extent of reduction achieved, each catalyst was passivated at room temperature in 1% O_2 after reduction and analysed using

© 2025 The Author(s). ChemCatChem published by Wiley-VCH GmbH

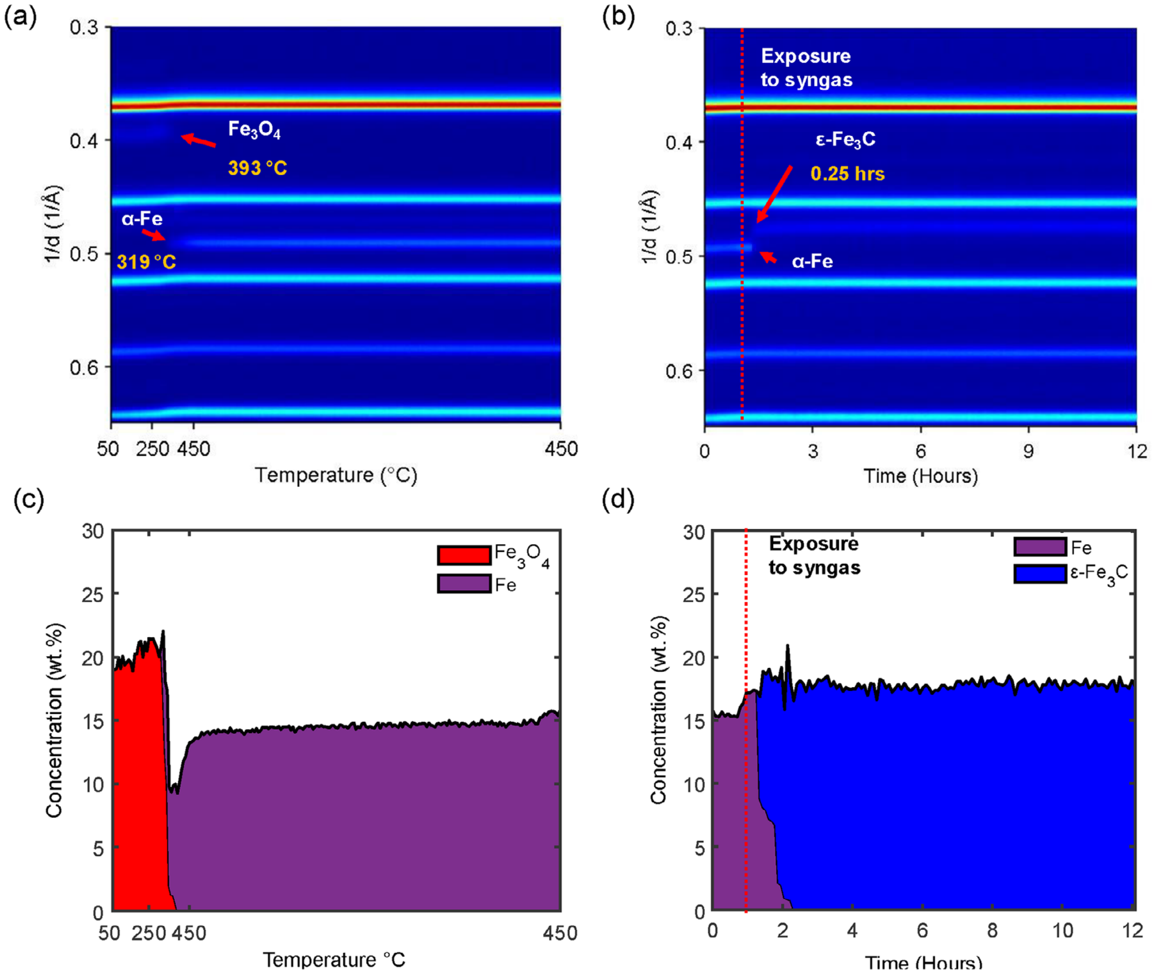

Figure 3. On-top view of XRD patterns collected as function of temperature and time. a) Reduction (H_2 flow, 450 °C, 15 h) and b) carburization ($H_2/CO = 2$, 240 °C, 15 bar) behavior of the unpromoted catalyst, K-2. c) The phase composition during reduction and d) carburization as calculated via Rietveld refinement is provided. All unlabeled reflections in (a & b) correspond to the perovskite phase. For clarity, the concentration of the perovskite phase is omitted in figure (c & d).

XRD. Similarly to the in situ XRD reduction studies, the resulting patterns confirmed complete transformation of the oxide phase to metallic Fe, as indicated by the characteristic reflections of Fe^0 at 0.493, 0.698, and 0.855 A^{-1} values, PDF-5+ 04–014–0164 (see Figure S5).

2.2. Fischer–Tropsch Activity and Selectivity

The catalytic performance of the potassium-promoted and unpromoted catalysts under FT synthesis conditions is summarized in Figures 4, S6 and S7, and Table S4. The CO conversion (orange circles, left y-axis) increased gradually with potassium loading from 38% to 53%, peaking for K-8 – despite a lower Fe^0 loading of 11 wt.%. This trend is attributed in part to a more rapid carburization as shown in the in situ XRD studies. Moreover, higher potassium levels boost intrinsic site activity of the carbide phase by donating electron density from the potassium metal to the iron phase, thereby enhancing CO over H_2 adsorption and weakening the C–O bond.[23–26,27]

Table 2. Crystallite sizes of iron phases during catalyst activation and carburization determined by Rietveld refinement.

Catalyst	Average crystallite size (nm)		
	Fresh[a)]	Reduced[b)]	Carburized[c)]
	Fe_3O_4	α-Fe	ε-Fe_3C
K-0	8.79	18.8	7.80
K-2	7.90	17.9	8.50
K-8	7.80	10.0	8.40

[a)] Determined at the beginning of the reduction experiment, at 50 °C.
[b)] Determined at the end of the reduction experiment, at 450 °C.
[c)] Determined at the end of the carburisation experiment, at 240 °C.

Water-gas shift activity increased progressively with potassium loading, as shown by the rise in CO_2 selectivity (grey bars, left y-axis, plotted in reverse) increasing from 27% of all carbon in the product (C-%) for the unpromoted catalyst, to 43 C-% for K-8. However, the increase is not linear but a near step type jump in WGS activity is recorded when increasing the potassium

© 2025 The Author(s). ChemCatChem published by Wiley-VCH GmbH

18673899, 0, Downloaded from https://chemistry-europe.onlinelibrary.wiley.com/doi/10.1002/cctc.202501430 by NICE, National Institute for Health and Care Excellence, Wiley Online Library on [13/01/2026]. See the Terms and Conditions (https://onlinelibrary.wiley.com/terms-and-conditions) on Wiley Online Library for rules of use; OA articles are governed by the applicable Creative Commons License

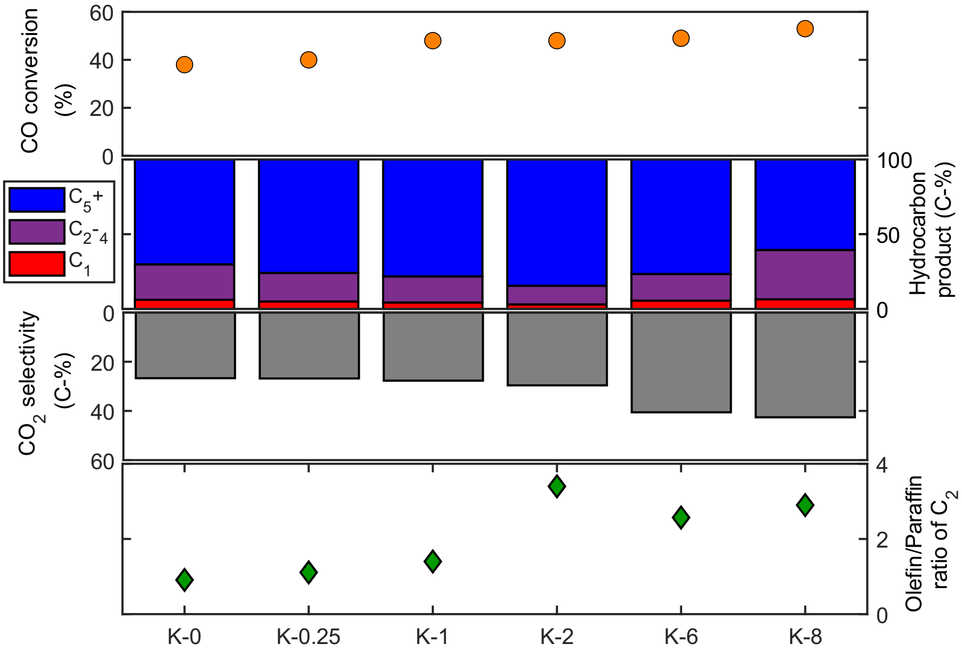

Figure 4. Catalyst performance of K-0, K-0.25, K-1, K-2, K-6, and K-8 catalysts run under Fischer-Tropsch conditions at 240 °C, 15 bar, $H_2/CO = 2$ for 48 h′ time on stream in a continuously stirred tank reactor. The first (top) panel displays the CO conversion, the stacked bar chart in the second panel showing the hydrocarbon fraction in the product stream. The third panel shows the WGS activity as selectivity towards CO_2 of these catalysts, and the fourth panel shows O/P ratio in the C_2 hydrocarbon fraction.

loading beyond 2 at.-% (Figures 4 and S8a). This is substantially higher than the values reported by Khasu et al.[13] (9–12 C-%), whose 22 nm γ-Fe_2O_3 nanoparticles prepared in the presence of chlorine ions may have inhibited WGS, compared to the catalysts prepared in the present study. Surprisingly, methane selectivity followed an inverted volcano trend, reaching a minimum of about 2 C-% for K-2, demonstrating that small amounts of potassium effectively inhibit methanation pathways. This optimum coincided with the highest C_5^+ selectivity (85 C-%) and the lowest formation of light hydrocarbons (12 C-%). While chain growth probabilities (α_1) remained relatively stable between 0.59 – 0.64, the observed shift in product distribution suggests a reduction in the chain termination probability (see Figure S8a). The C_2 olefin-to-paraffin (O/P) ratio is only mildly affected at low potassium concentrations but steps to a maximum at 2 at.% K in the A site of the perovskite (Figures 4 and S7). At higher potassium loadings (>2 at.%), the O/P ratio decreases slightly. Notably, the O/P ratio of higher hydrocarbons is hardly affected by the presence of K (Figure S8b).

X-ray diffraction of the spent catalysts confirmed that the perovskite support remained structurally intact during FT reaction conditions, with no phase changes detected (see Figure S9). All catalysts showed reflections corresponding to an iron carbide phase with minor contribution from metallic Fe^0 and magnetite, suggesting limited reoxidation under reaction conditions.

Having previously shown that perovskite-based systems are effective supports for FT catalysts, we have selected K-2, the best-performing catalyst in terms of long chain hydrocarbon selectivity, for further structural investigation. The local potassium environment was probed using thermal alkali desorption studies and X-ray absorption spectroscopy (XAS).

2.3. Characterising Potassium Speciation

Thermal alkali desorption studies of the as-synthesised K-2 support revealed distinct potassium release features from around 450 °C, with two overlapping features near between 500 and 575 °C (Figures 5a and S10a). These desorption events likely represent potassium species occupying different coordination environments and exhibiting varying binding strengths (Figure 5a). Notably, these species are absent when cooling the sample back to 400 °C (Figure S10a). At higher potassium loading, K-8 demonstrates no significant alkali desorption below 550 °C (Figures 5a and S10c). The heating and cooling profiles overlapped closely across the entire temperature range (Figure S10c). For a $LaAl_{0.8}Mn_{0.2}O_{3-\delta}$ perovskite bearing 0.36 wt.% potassium (equivalent in mass to the 2 at.% replacement of the A site) introduced via impregnation (see Figure S10e), the desorption profile in the calcined state (Figure 5a) suggests an intermediate binding strength of potassium to the surface of the perovskite when compared to the K-2 and K-8 samples.

After a reductive treatment, mimicking catalyst activation before exposure to FT conditions, no difference between the potassium desorption from the empowered supports, K-2 and K-8, is apparent (Figures 5b and S10 b,d). The absence of alkali species leaving the surface below 550 °C suggests a strong surface binding strength as would be expected for potassium incor-

© 2025 The Author(s). ChemCatChem published by Wiley-VCH GmbH

18673899, 0, Downloaded from https://chemistry-europe.onlinelibrary.wiley.com/doi/10.1002/cctc.202501430 by NICE, National Institute for Health and Care Excellence, Wiley Online Library on [13/01/2026]. See the Terms and Conditions (https://onlinelibrary.wiley.com/terms-and-conditions) on Wiley Online Library for rules of use; OA articles are governed by the applicable Creative Commons License

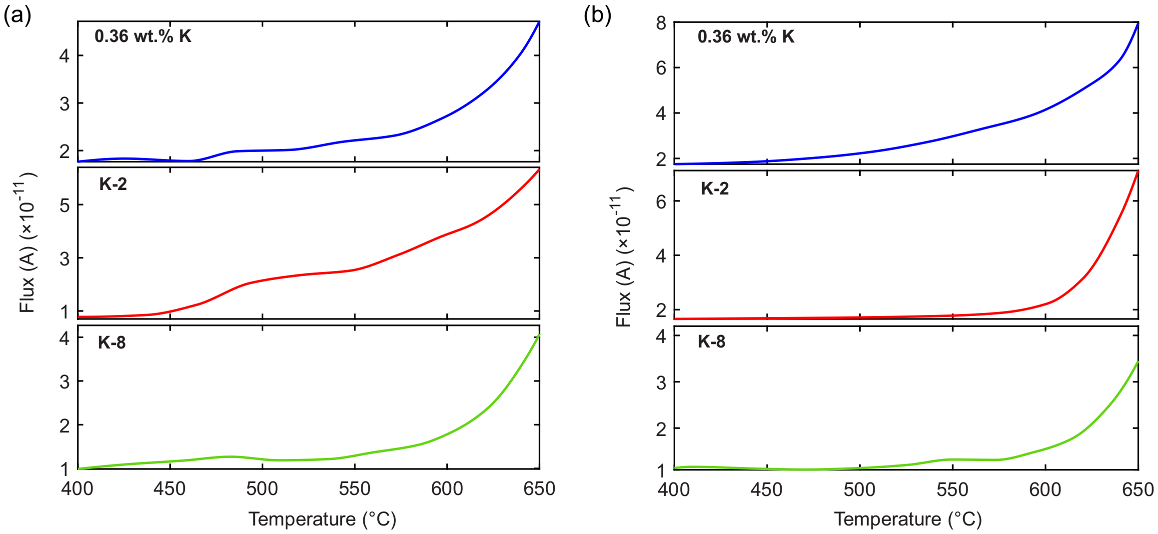

Figure 5. Potassium desorption flux *as* a function of temperature *for* the 0.36 wt.% K- $LaAl_{0.8}Mn_{0.2}O_{3\delta}$ (blue), K-2 (red), and K-8 (green) during the heating *of* the a) calcined and b) reduced samples.

porated into the crystal lattice of the perovskite. This observation further supports the hypothesis that potassium undergoes a change in speciation, with the reduction driving lattice incorporation as previously reported by Khasu et al.[13] When compared with potassium impregnated onto the surface of a perovskite (Figure S10f), it is evident that the impregnated alkali species are much less strongly bound to the perovskite surface, with desorption events observed from 450 °C onwards.

The thermal alkali desorption studies suggest that after the reductive treatment, the potassium species in the perovskite lattice are more strongly bound compared to potassium impregnated onto the surface of the $LaAl_{0.8}Mn_{0.2}O_{3\text{-}\delta}$. At the lowest potassium concentrations, sample K-2, the potassium speciation changes during the reductive treatment, transitioning from species of varying bonding strength to species that effectively desorb in a single event at temperatures beyond 600 °C, largely mirroring the behavior of K-8. In our previous study,[13] we identified the role of the Mn oxidation state to counteract the charge imbalance introduced by the incorporation of K^+ in the A site of the crystal lattice. In the absence of Mn this charge balancing was achieved through a partial reduction of the perovskite lattice creating oxygen vacancies stabilizing potassium. To investigate if the low concentration of alkali in K-2 does not introduce sufficient charge imbalance to require the Mn to change its oxidation state, X-ray absorption experiments of the La K and L_3-edge, the Mn K-edge and the K K-edge were carried out at the beamline BM28 of the European Synchrotron Radiation Facility (ESRF).

Potassium K-edge X-ray Absorption Near Edge Spectroscopy (XANES) has previously been shown to exhibit rich features that are highly sensitive to the local structure of potassium, making it a valuable technique to probe its bulk environment within the K-2 support (Figure 6).[13,28,29] Although the spectra have low signal-to-noise ratio due to the low potassium concentration, the features observed before and after reduction closely resemble those reported for higher potassium loadings in the same perovskite lattice. Specifically, the XANES shows a preedge feature at 3613 eV and a broad feature at 3617 eV, although these are less well resolved and more convoluted in the K-2 sample compared with $La_{0.9}K_{0.1}Al_{0.4}Mn_{0.6}O_3$ spectra.[13] The XANES fingerprint of the $La_{0.9}K_{0.1}Al_{0.4}Mn_{0.6}O_3$ perovskite, supported by Extended X-ray Absorption Fine Structure (EXAFS) analysis, has been classified as indicative of potassium occupying the A site of the perovskite lattice.[13] Although EXAFS was not feasible for the K-2 support, the similarity in the XANES strongly suggests that potassium is in a comparable bulk environment. The XANES also differ from K_2CO_3 (features at 3614 and 3621 eV), indicating that no bulk external framework potassium phase was present

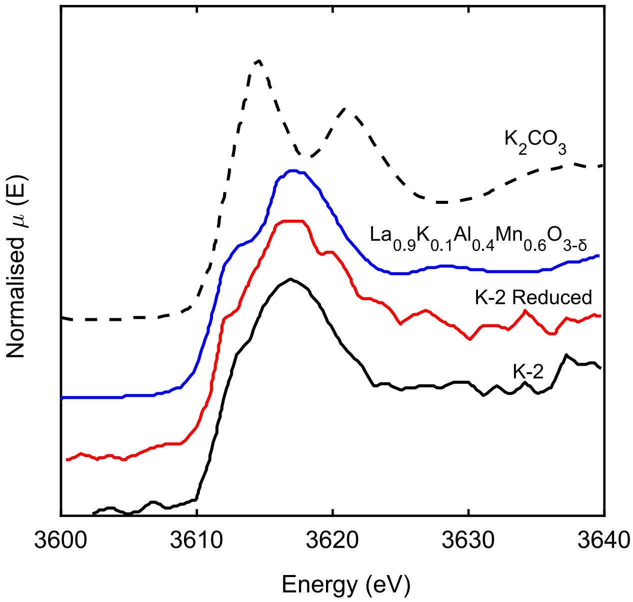

Figure 6. Potassium K-edge XANES of perovskite catalyst supports; K-2 (black), K-2 reduced (red), and $La_{0.9}K_{0.1}Al_{0.4}Mn_{0.6}O_{3\text{-}\delta}$ (blue). The spectrum of K_2CO_3 is provided reference (adapted from.[13])

© 2025 The Author(s). ChemCatChem published by Wiley-VCH GmbH

18673899, 0, Downloaded from https://chemistry-europe.onlinelibrary.wiley.com/doi/10.1002/cctc.202501430 by NICE, National Institute for Health and Care Excellence, Wiley Online Library on [13/01/2026]. See the Terms and Conditions (https://onlinelibrary.wiley.com/terms-and-conditions) on Wiley Online Library for rules of use; OA articles are governed by the applicable Creative Commons License

Table 3. Fitting of La L_3-edge XANES. Fitting performed using a fixed arc-tangent to replicate the edge step. Step of 0.85, width 1.03 eV and an E_0 of 5488.7 Ev.

Sample	FWHM (eV)	Centre (eV)	R-factor (10^{-4})
K-0	5.1 (2)	5491.0	55
K-2	5.0 (1)	5491.0	76
K-2 reduced	5.2 (1)	5490.9	57

in the low loaded perovskite samples.[13,28] However, the broadening of features in the XANES may indicate a range of subtly different environments. Importantly, XAS is a bulk averaging technique and cannot rule out a small fraction of minor surface potassium species. Nevertheless, it supports XRD observations that most of the potassium is incorporated into the perovskite lattice.

Extended X-ray Absorption Fine Structure of the lanthanum K-edge (see Figure S11) reinforces the XRD findings that the perovskite supports are crystalline and that there is no significant contribution of La present as isolated carbonate or oxide phases, either in the reference potassium-free sample or in K-2 before and after reduction. Many scattering paths associated with first and second shell La–O, La-Al/Mn first shell and La-La first and second shells in the perovskite lattice were observed. Counter-intuitively this made EXAFS fitting challenging and unnecessary, given the clear evidence from comparison of simulated scattering paths (see Figure S12) with experiment that the La is within the perovskite lattice. Analysis of the FWHM of the white line in the lanthanum L_3-edge (see Figure S13 and Table 3), which is sensitive to coordination number and distortions in the local coordination geometry, further supports that the average La coordination is 12 as expected on the A site of the perovskite lattice.

Manganese K-edge XANES was used to identify how the Mn oxidation state was influenced by potassium incorporation to K-2. Previous 10% A site substitution of La^{+3} with K^+ resulted in an increase in Mn oxidation state, as seen by a −0.7 eV shift in the edge position relative to an unsubstituted perovskite (see Figure S14). The oxidation of Mn is required to compensate for the charge imbalance created by the net reduction in A site oxidation state. The observed shift in Mn oxidation state was attributed to the perovskite being able to readily accommodate K^+ into the lattice, as in the absence of Mn (i.e., a $La_{0.9}K_{0.1}AlO_3$) evidence of potassium surface enrichment and K_2CO_3 was observed.[13] In the absence of Mn, the creation of oxygen vacancies on sample reduction was required to facilitate K^+ substitution. No shift in edge position at 6554.4 eV was observed between the K-2 and the potassium-free perovskite (Figure 7), indicating that the lower level of A site doping was insufficient to alter the bulk Mn oxidation state. Alternatively, the reduced driving force for K^+ substitution at low loading may explain the absence of a shift. As observed with higher K^+ substitution, the Mn edge position shifted lower by 6554 eV on sample reduction. Such a reduction being attributed to Mn moderating the charge imbalance created by oxygen vacancies, which also stabilises K^+ substitution into the lattice.

3. Conclusion

The presented findings confirm that empowered supports can enhance iron-based FT activity and selectivity and specifically that the potassium concentration in the perovskite lattice can be tuned to optimise product composition. A moderate potassium loading of 2 at.-% in the A site of the perovskite (K-2) provided the optimal balance of catalytic performance, yielding maximum C_{5+} selectivity and suppressed methane formation, within the synthesized samples. Thermal alkali desorption studies revealed that this loading also coincided with the most dynamic potassium behavior, characterized by distinct desorption features in the calcined state that were altered upon reduction, consistent with potassium species loosely associated with the perovskite structure that become more strongly bound after reduction. After a reductive treatment, equating the activation procedure before exposure to FT conditions, potassium species exhibited much stronger binding strength compared to conventionally impregnated species. While XAS studies of the K-2 sample could not elucidate the exact nature of the potassium species, the analysis of the oxidation state of Mn provides a possible explanation for the different bonding strength of the alkali before and after reductive treatment. We have previously observed, at higher potassium concentrations, that Mn assists in overcoming the charge imbalance induced by replacing La^{3+} with K^+. At the low loadings of K-2 no significant change in oxidation state of the manganese is observed, resulting in a locally strained system. Upon reduction, the average manganese oxidation state decreases, reducing the lattice and strengthening the binding of the potassium species. This behavior coincides with the observed advantageous catalyst selectivity, although no detailed explanation for this correlation can be provided at this stage. Lower potassium concentrations in the empowered supports (K-0.25 and K-1) only show a moderate enhancement of the FT selectivity, predominantly regarding chain growth. The K-2 supports the highest chain growth probability of the tested samples, supressed secondary hydrogenation as evidence by the olefin to paraffin ratio but does not enhance water gas shift activity, as observed at higher potassium concentration. Collectively, this work demonstrates that the fine-tuning of the potassium loading in empowered support structures can optimize the structural evolution of the active phase and improve the overall FTS activity of these designed catalysts.

4. Experimental Section

4.1. Synthesis of Fe_3O_4 Nanoparticles

Iron oxide (Fe_3O_4) nanoparticles were synthesised via a modified co-precipitation method previously described by Fadlalla et al.[30] In short, a 0.2 M aqueous solution of $Fe(NO_3)_3{\cdot}9H_2O$ and a 0.1 M of $FeCl_2{\cdot}4H_2O$ (both Sigma-Aldrich) were prepared separately in near-boiling deionised water. Equal volumes (50 mL) of each precursor solution were simultaneously added to 1.3 L of vigorously stirred, near-boiling sodium hydroxide solution (35.35 g NaOH in deionised water). The addition of the metal precursors resulted in immediate precipitation of a black solid, attributed to Fe_3O_4 formation. The

© 2025 The Author(s). ChemCatChem published by Wiley-VCH GmbH

18673899, 0, Downloaded from https://chemistry-europe.onlinelibrary.wiley.com/doi/10.1002/cctc.202501430 by NICE, National Institute for Health and Care Excellence, Wiley Online Library on [13/01/2026]. See the Terms and Conditions (https://onlinelibrary.wiley.com/terms-and-conditions) on Wiley Online Library for rules of use; OA articles are governed by the applicable Creative Commons License

18673899, 0, Downloaded from https://chemistry-europe.onlinelibrary.wiley.com/doi/10.1002/cctc.202501430 by NICE, National Institute for Health and Care Excellence, Wiley Online Library on [13/01/2026]. See the Terms and Conditions (https://onlinelibrary.wiley.com/terms-and-conditions) on Wiley Online Library for rules of use; OA articles are governed by the applicable Creative Commons License

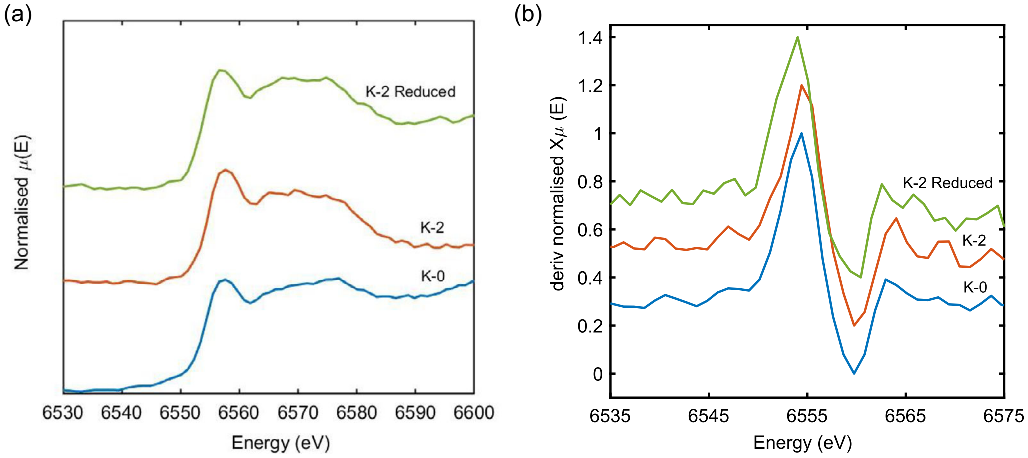

Figure 7. Mn K-edge XANES of perovskite supports; K-0 (blue), K-2 (red), and K-2 reduced (green). a) XANES of supports; b) derivative of XANES spectra illustrating the shift in E_0 upon reductive treatment.

reaction mixture was maintained at 95 °C for 1 h to promote crystallisation of the spinel structure. Afterwards, the mixture was allowed to cool slowly to room temperature, allowing the solid to settle. The supernatant was carefully decanted, and the precipitate was washed repeatedly with cold deionised water until the filtrate reached neutral pH. The final product was air dried at room temperature and subsequently characterized.

4.2. Synthesis of $La_{1-x}K_xAl_{0.8}Mn_{0.2}O_{3-\delta}$ Perovskites

$LaAl_{0.8}Mn_{0.2}O_{3-\delta}$ perovskites were prepared via a citrate-nitrate combustion method using $La(NO_3)_3{\cdot}6H_2O$, $Al(NO_3)_3{\cdot}9H_2O$, $Mn(NO_3)_2{\cdot}4H_2O$, $C_6H_8O_7{\cdot}H_2O$, $(CH_2OH)_2$, (all Sigma-Aldrich 99%–99.99% purity), HNO_3 and deionized water.[31] The precursor solution was prepared by dissolving the metal nitrates and citric acid in deionized water in a 250 mL round-bottom flask. The solution was ultrasonicated to achieve complete dissolution, after which nitric acid was added. The molar ratio of citric acid to the metal cations was 2:1. The solution was stirred using a magnetic stirrer and heated to 60 °C. Ethylene glycol was added to the above solution in the molar ratio of 3:1 with respect to citric acid. The resulting solution was heated on a hot plate to about 90 °C for 1.5 h, producing a viscous gel, then dried at 350 °C to initiate polymerisation and partial decomposition. The gel undergoes dehydration to form a polymer complex, followed by decomposition with enormous swelling, producing a foam which auto-combusts, to form a fine black powder. The precursor powder was well ground with an agate mortar and calcined at 800 °C for 6 h in an oven (ramp rate of 2 °C/min). The procedure was followed for the preparation of potassium-substituted materials, $La_{1-x}K_xAl_{0.8}Mn_{0.2}O_{3-\delta}$, ($x$ is $\leq$ 8 at.%), by replacing part of La precursor with KNO_3 (Sigma–Aldrich) at the desired stoichiometry. Table 4 provides the naming convention adopted for the synthesised catalysts.

4.3. Supporting Fe_3O_4 Nanoparticles

The synthesized iron oxide nanoparticles were deposited onto the perovskite materials via a physical mixing method targeting a 15 wt.% loading of Fe.[32] The nanoparticles and support were dispersed in deionized water and ultrasonicated for 1 h to minimize agglomeration. The resulting suspension was transferred to a rotary evaporator and dried at 60 °C and 72 mbar for 3 h. To ensure complete removal of moisture, the partially dried material was subsequently placed in an oven at 60 °C for an additional 2 h.

4.4. Catalysts Characterization

4.4.1. X-Ray Diffraction (XRD)

The crystallographic structure of the synthesized materials was analyzed using powder XRD. The data was acquired using a Bruker AXS D8 Advance X-ray laboratory diffractometer operated at 35 kV and 40 mA using a cobalt source and a LynxEye position sensitive detector (Bruker AXS). Analysis was performed with a scan range of 20–120 ° 2θ, a step-size of 0.01 ° and a scan rate of 0.025 °/s. The diffraction patterns of the samples obtained were analyzed against reference entries in the PDF-5 database.

4.4.2. Transmission Electron Microscopy (TEM)

The as-synthesized perovskites, fresh and spent catalyst were characterized using transmission electron microscopy. A Tecnai F20 TEM equipped with a field emission gun operated at 200 kV was used to determine the size distribution and morphology of the prepared samples. For sample preparation, a small volume of solid was suspended in ethanol using ultrasonication. A droplet of the supernatant was transferred onto a holey carbon-coated copper grid and dried in air for about 10 min before analysis. The obtained micrographs were analyzed with the freeware ImageJ to obtain particle size distributions. For statistical relevance about 200–250 particles were counted for each sample.

4.4.3. Surface Area Measurements via N_2 Adsorption

The specific surface area and pore size distribution of the support was determined using the Brunauer-Emmett-Teller (BET) method based on the physical adsorption and capillary condensation (Micromeritics TriStar 3000). The samples were cooled to liquid nitrogen temperature, followed by physical absorption (based on van der Waals interactions) of N_2 molecules from a known amount of gas onto the surface of the sample. From the amount of adsorbed gas, assuming monomolecular coverage, a surface area can be extracted.

© 2025 The Author(s). ChemCatChem published by Wiley-VCH GmbH

Table 4. List of prepared perovskite supports, and naming convention tested under Fischer-Tropsch reaction conditions.

Catalyst	Targeted potassium content (at.%)	Catalyst nomenclature
$LaAl_{0.8}Mn_{0.2}O_{3-\delta}$	0	K-0
$La_{0.9975}K_{0.0025}Al_{0.8}Mn_{0.2}O_{3-\delta}$	0.25	K-0.25
$La_{0.995}K_{0.005}Al_{0.8}Mn_{0.2}O_{3-\delta}$	0.5	K-0.5
$La_{0.99}K_{0.01}Al_{0.8}Mn_{0.2}O_{3-\delta}$	1	K-1
$La_{0.985}K_{0.015}Al_{0.8}Mn_{0.2}O_{3-\delta}$	1.5	K-1.5
$La_{0.98}K_{0.02}Al_{0.8}Mn_{0.2}O_{3-\delta}$	2	K-2
$La_{0.96}K_{0.04}Al_{0.8}Mn_{0.2}O_{3-\delta}$	4	K-4
$La_{0.94}K_{0.06}Al_{0.8}Mn_{0.2}O_{3-\delta}$	6	K-6
$La_{0.92}K_{0.08}Al_{0.8}Mn_{0.2}O_{3-\delta}$	8	K-8

4.4.4. Inductively Coupled Plasma Optical Emission Spectrometry (ICP-OES)

For microwave-assisted acid digestion, the samples were mixed with 5 mL HNO_3, 2 mL HCl, 3 mL H_2SO_4, and 1 mL Aqua Regia. The samples were ramped up to 220 °C in 30 min and this temperature was held for 1 h. Following digestion, each solution was transferred to a 50 mL volumetric flask and topped up with 2 wt.% HNO_3. Prior to the dilution the samples were filtered using a 0.2 µm filter. Thereafter 1 mL of the sample was pipetted into a 10 mL volumetric flask and topped up with 2 wt.% HNO_3. The solution was injected into a Varian ES 730 ICP-OES Mars 6 Microwave Digester instrument as an aerosol where it was ionized as it passed through the plasma. Upon returning to the ground state, the atoms emit energy which the instrument records in wavelength and intensity.

4.4.5. In Situ X-Ray Diffraction

Catalyst reduction and carburization studies were performed on a Bruker D8 Advance diffractometer equipped with a molybdenum source ($\lambda = 0.7093$ nm) and a VANTEC-2000 position-sensitive detector (Bruker AXS). A custom-built capillary cell developed at the University of Cape Town was used to monitor real-time structural changes under reduction and reaction conditions.[33] Reduction was carried out in flowing H_2 (5 mL/min), heating the sample to 450 °C at 2 °C/min, and holding it for 15 h. Scans were collected from 12° to 27° 2θ every 4 min, with a 59-s delay between scans. Following reduction, the system was cooled to 240 °C, pressurized from ambient to 15 bar, and switched to syngas gas ($H_2/CO = 2$). The catalyst phase changes were monitored under these conditions for 24 h, and diffraction data was analyzed by comparison to standard patterns. Phase quantification was obtained through Rietveld refinement using the TOPAS 5 software package.[34]

4.4.6. Thermal Alkali Desorption Studies

Studies on the potassium surface states in the calcined and reduced perovskite supports without iron nanoparticles were carried out using the species-resolved thermal alkali desorption (SR-TAD) at the Department of Inorganic Chemistry, Faculty of Chemistry, Jagiellonian University (Kraków, Poland). In SR-TAD, heating an alkali-containing catalyst allows determination of desorption activation energies, temperature ranges and quantifications of desorbing species. The potassium thermal desorption experiments were conducted in a vacuum apparatus with a background pressure of 10^{-7} mbar. Catalyst powders were pressed into 13 mm diameter discs and heated stepwise from ambient temperature to 700 °C in approximately 10 °C per step. Desorbing potassium atom were ionized on a surface-ionization detector (SID), and the resulting positive current was measured directly by a Keithley 6512 digital electrometer.

4.4.7. X-ray Adsorption Spectroscopy

XAS measurements were carried out at the beamline BM28 of the ESRF, Grenoble, France. Measurements were conducted on pelletized or wax-embedded samples in the following states: as prepared, H_2 reduced (and passivated), Spectra at the La K-edge, La L_3-edge, Mn K-edge, and K K-edge were recorded. Fluorescence detection was employed for K and Mn K-edges and La L_3 edge due to the low absorber concentration, while and La K edge was recorded in transmission mode after diluting 1:15 with crystalline cellulose. To improve the signal-to-noise ratio, each sample was scanned multiple times, and the scans were averaged. Energy calibration and edge-feature assignment were achieved by measuring $LaCO_3OH$, $La_2O_2CO_3$, La_2O_3 and KCl reference salts. Data reduction, energy alignment, and normalization were performed in Athena (Demeter).

4.4.8. Fischer-Tropsch Synthesis and Product Analysis

Catalyst activation was performed in a fixed-bed quartz reactor, where 5 g of supported catalyst (80 wt.% perovskite support and 20 wt.% Fe_3O_4 nanoparticles) was reduced under H_2 flow (80 mL/min) at 450 °C for 15 h (ramp rate 2 °C/min). After cooling to room temperature, the reduced catalyst was embedded in 20 g of molten Sasol H1 wax (under Ar atmosphere) and allowed to solidify. The wax-encapsulated catalyst was then transferred into a 600 mL continuously stirred tank reactor (slurry reactor) loaded with 330 g of molten wax at 140 °C. The reactor was sealed, pressurized to 15 bar with argon, and heated to the reaction temperature of 240 °C while stirring at 350 rpm. FT synthesis was initiated by feeding syngas ($H_2/CO = 2$) containing 10 vol.% N_2 at 0.48 $L/h.g_{catalyst}$. Permanent gases were continuously analyzed using a GC equipped with a thermal conductivity detector (Agilent 7820A), while hydrocarbons products were collected in evacuated ampoules [35] and analyzed offline by a gas chromatograph equipped with a flame ionization detector (Varian CP3800). Methane was used as an internal standard to correlate both datasets.

© 2025 The Author(s). ChemCatChem published by Wiley-VCH GmbH

18673899, 0, Downloaded from https://chemistry-europe.onlinelibrary.wiley.com/doi/10.1002/cctc.202501430 by NICE, National Institute for Health and Care Excellence, Wiley Online Library on [13/01/2026]. See the Terms and Conditions (https://onlinelibrary.wiley.com/terms-and-conditions) on Wiley Online Library for rules of use; OA articles are governed by the applicable Creative Commons License

Acknowledgments

The authors acknowledge the financial contributions from c*change (DSTI-NRF Centre of Excellence in Catalysis) and the National Research Fund (NRF) through the SARChI in Sustainable Catalysis (UID: 150528). We further acknowledge Mohamed Jaffer and Miranda Waldron at the Electron Microscope Units for their support and assistance with TEM imaging and SEM-EDX mapping, Dr Mohamed Fadlalla and Dr Shaine Raseale for assistance with data analysis, the Analytical Laboratory in the Department of Chemical Engineering at UCT for ICP-OES and BET surface area measurements. S.A.K. and E.B.M. acknowledge the financial contribution from the EPSRC (EP/Z535989/1) XAFS analysis was performed at BM28 (XMaS) at the European Synchrotron Radiation Facility using the CRG route (A28-1-1394). XMaS is a UK national research facility supported by the EPSRC. We are grateful to all the beamline team staff, particularly Laurence Bouchenoire for their support.

Conflict of Interests

The authors declare no conflict of interest.

Data Availability Statement

The data that support the findings of this study are available from the corresponding author upon reasonable request.

Keywords: Empowered supports · Fischer-Tropsch synthesis · Iron catalyst · Perovskites · Potassium

[1] J. W. Niemantsverdriet, A. M. van der Kraan, *J. Catal.* **1981**, *72*, 385–388, https://doi.org/10.1016/0021-9517(81)90025-7.
[2] M. E. Dry, *Stud. Surf. Sci. Catal.* **2004**, *152*, 533–600.
[3] A. Nakhaei Pour, M. R. Housaindokht, J. Zarkesh, S. F. Tayyari, *J. Indus. Eng. Chem.* **2010**, *16*, 1025–1032, https://doi.org/10.1016/j.jiec.2010.09.003.
[4] F. E. M. Farias, R. C. R. Neto, M. A. S. Baldanza, M. Schmal, F. A. N. Fernandes, *Braz. J. Chem. Eng.* **2011**, *28*, 495–504, https://doi.org/10.1590/S0104-66322011000300015.
[5] Y. Yang, H.-W. Xiang, Y.-Y. Xu, L. Bai, Y.-W. Li, *Appl Catal A Gen* **2004**, *266*, 181–194, https://doi.org/10.1016/j.apcata.2004.02.018.
[6] H. Schulz, *Catal. Today* **2014**, *228*, 113–122, https://doi.org/10.1016/j.cattod.2013.11.060.
[7] A. Lappas, E. Heracleous, *Handbook of Biofuels Production*, Woodhead Publishing Limited Cambridge, USA **2011**.
[8] V. Subramanian, K. Cheng, Y. Wang, *Reference Module in Chemistry, Molecular Sciences and Chemical Engineering*, Elsevier **2017**.
[9] V. R. R. Pendyala, U. M. Graham, G. Jacobs, H. H. Hamdeh, B. H. Davis, *Catal Letters* **2014**, *144*, 1704–1716, https://doi.org/10.1007/s10562-014-1336-z.
[10] G. Connell, J. A. Dumesic, *J. Catal.* **1985**, *92*, 17–24, https://doi.org/10.1016/0021-9517(85)90233-7.
[11] J. Li, X. Cheng, C. Zhang, J. Wang, W. Dong, Y. Yang, Y. Li, *J. Chemical Technol. & Biotechnol.* **2017**, *92*, 1472–1480, https://doi.org/10.1002/jctb.5152.
[12] M. Z. L. L. Ribeiro, J. C. Souza, I. F. Gomes, M. K. Gnanamani, M. Martinelli, G. Jacobs, M. C. Ribeiro, *Catalysts* **2024**, *14*, 682, DOI https://doi.org/10.3390/catal14100682.
[13] M. Khasu, W. Marquart, P. J. Kooyman, C. Drivas, M. A. Isaacs, A. J. Mayer, S. E. Dann, S. A. Kondrat, M. Claeys, N. Fischer, *ACS Catal.* **2023**, *13*, 6862–6872, https://doi.org/10.1021/acscatal.3c00924.
[14] L. Bedel, A. C. Roger, J. L. Rehspringer, A. Kiennemann, in *Natural Gas Conversion VII* (Eds: X. Bao, Xu. Yidu), Elsevier Oxford, UK **2004**, pp. 319–324.
[15] L. Bedel, A. C. Roger, J. L. Rehspringer, Y. Zimmermann, A. Kiennemann, *J. Catal.* **2005**, *235*, 279–294, https://doi.org/10.1016/j.jcat.2005.07.025.
[16] B. Moshtari, S. H. Hashemabadi, Y. Zamani, *Sci Rep* **2024**, *14*, 9189, DOI https://doi.org/10.1038/s41598-024-59561-y.
[17] A.-C. Roger, A. Kiennemann, in *Perovskites and Related Mixed Oxides*, John Wiley & Sons, Ltd Weinheim, Germany **2016**, pp. 631–658, https://doi.org/10.1002/9783527686605.
[18] S. Cimino, L. Lisi, S. De Rossi, M. Faticanti, P. Porta, *Appl. Catal. B* **2003**, *43*, 397–406, https://doi.org/10.1016/S0926-3373(03)00023-7.
[19] L. Niu, X. Liu, X. Liu, Z. Lv, C. Zhang, X. Wen, Y. Yang, Y. Li, J. Xu, *ChemCatChem* **2017**, *9*, 1691–1700.
[20] F. E. M. Farias, R. C. Rabelo Neto, M. A. S. Baldanza, M. Schmal, F. A. N. Fernandes, *Braz. J. Chem. Eng.* **2011**, *28*, 495–504.
[21] H. Chang, Q. Lin, M. Cheng, K. Zhang, B. Feng, J. Chai, Y. Lv, Z. Men, *Catalysts* **2022**, *12*, 916, DOI https://doi.org/10.3390/catal12080916.
[22] X. Liu, C. Zhang, Y. Li, J. W. Niemantsverdriet, J. B. Wagner, T. W. Hansen, *ACS Catal.* **2017**, *7*, 4867–4875, https://doi.org/10.1021/acscatal.7b00946.
[23] A. J. Barrios, B. Gu, Y. Luo, D. V. Peron, P. A. Chernavskii, M. Virginie, R. Wojcieszak, J. W. Thybaut, V. V. Ordomsky, A. Y. Khodakov, *Appl. Catal. B* **2020**, *273*, 119028, https://doi.org/10.1016/j.apcatb.2020.119028.
[24] Z. Tao, Y. Yang, H. Wan, T. Li, X. An, H. Xiang, Y. Li, *Catal Letters* **2007**, *114*, 161–168, https://doi.org/10.1007/s10562-007-9060-6.
[25] Z. Tian, C. Wang, J. Yue, X. Zhang, L. Ma, *Catal. Sci. Technol.* **2019**, *9*, 2728–2741, https://doi.org/10.1039/C9CY00403C.
[26] J. X. Liu, P. Wang, W. Xu, E. J. M. Hensen, *Engineering* **2017**, *3*, 467–476, https://doi.org/10.1016/J.ENG.2017.04.012.
[27] E. I. Mabaso, E. van Steen, M. Claeys, *DGMK Tagungsbericht* **2006**, *4*, 93–100.
[28] C. J. Davies, A. Mayer, J. Gabb, J. M. Walls, V. Degirmenci, P. B. J. Thompson, G. Cibin, S. Golunski, S. A. Kondrat, *Phys. Chem. Chem. Phys.* **2020**, *22*, 18976–18988, https://doi.org/10.1039/D0CP01227K.
[29] A. J. Mayer, O. T. Beynon, A. J. Logsdail, K. G. Upul Wijayantha, S. E. Dann, J. Jos´, J. F. Marco, J. D. Elliott, M. Aramini, G. Cibin, S. A. Kondrat, *J. Mater. Chem. A* **2023**, *11*, 19900-19913, DOI https://doi.org/10.17172/NOMAD/2023.07.25-1.
[30] M. I. Fadlalla, S. Ganesh Babu, T. M. Nyathi, C. J. Kees-Jan Weststrate, N. Fischer, J. W. Hans Niemantsverdriet, M. Claeys, *ACS Catal.* **2020**, *10*, 14661–14677, https://doi.org/10.1021/acscatal.0c03346.
[31] U. Megha, K. Shijina, G. Varghese, *Process. Appl. Ceram.Processing and Application of Ceramics* **2014**, *8*, 87–92.
[32] N. Fischer, E. van Steen, M. Claeys, *Catal. Today* **2011**, *171*, 174–179, https://doi.org/10.1016/j.cattod.2011.03.018.
[33] N. Fischer, M. Claeys, *Catal. Today* **2016**, *275*, 149–154, https://doi.org/10.1016/j.cattod.2016.03.003.
[34] A. A. Coelho, *Appl. Crystallograph.* **2003**, *36*, 86–95, https://doi.org/10.1107/S0021889802019878.
[35] H. Schulz, W. Böhringer, C. P. Kohl, N. M. Rahman, A. Will, *German Society for Petroleum and Coal Chemistry* **1984** *3*, 320-329.

Manuscript received: September 18, 2025
Revised manuscript received: November 1, 2025
Accepted manuscript online: November 23, 2025
Version of record online: ■■, ■■

© 2025 The Author(s). ChemCatChem published by Wiley-VCH GmbH

18673899, 0, Downloaded from https://chemistry-europe.onlinelibrary.wiley.com/doi/10.1002/cctc.202501430 by NICE, National Institute for Health and Care Excellence, Wiley Online Library on [13/01/2026]. See the Terms and Conditions (https://onlinelibrary.wiley.com/terms-and-conditions) on Wiley Online Library for rules of use; OA articles are governed by the applicable Creative Commons License